Acta Materialia 224 (2022) 117490

Contents lists available at ScienceDirect

Acta Materialia

journal homepage: www.elsevier.com/locate/actamat

Full length article

Atomic-scale evidence of chemical short-range order in CrCoNi medium-entropy alloy

Lingling Zhou[a,b,†], Qi Wang[c,†], Jing Wang[a], Xuefei Chen[a,b], Ping Jiang[a], Hao Zhou[d], Fuping Yuan[a,b], Xiaolei Wu[a,b,*], Zhiying Cheng[e,*], En Ma[f,*]

[a] State Key Laboratory of Nonlinear Mechanics, Institute of Mechanics, Chinese Academy of Sciences, Beijing 100190, China
[b] School of Engineering Science, University of Chinese Academy of Sciences, Beijing 100049, China
[c] Science and Technology on Surface Physics and Chemistry Laboratory, P. O. Box 9-35, Jiangyou 621908, China
[d] Nano and Heterogeneous Materials Center, School of Materials Science and Engineering, Nanjing University of Science and Technology, Nanjing 210094, China
[e] National Center of Electron Microscopy in Beijing, School of Materials Science and Engineering, Tsinghua University, Beijing 100084, China
[f] Center for Alloy Innovation and Design (CAID), State Key Laboratory for Mechanical Behavior of Materials, Xi'an Jiaotong University, Xi'an 710049, China

ARTICLE INFO

Article history:
Received 6 July 2021
Revised 25 October 2021
Accepted 14 November 2021
Available online 17 November 2021

Keywords:
Chemical short-range order
High-entropy alloy
Microstructure

ABSTRACT

High (or medium)-entropy alloys (H/MEAs) are complex concentrated solid solutions that may develop chemical short-range order (CSRO). In this regard, CrCoNi, the prototypical face-centered-cubic MEA, has recently kindled a debate in the H/MEA community, as it is uncertain if CSRO can possibly form in such a multi-principal-element solution, where no equilibrium or metastable intermetallic compounds have ever been seen or predicted. To answer this challenging question, here we present firm experimental evidence for the CSRO from electron diffraction as well as atomic-resolution chemical mapping, under an appropriate zone axis. We also develop a methodology to reliably determine the locations of atomic columns from the line scan profiles in the chemical maps, as well as a quantitative covariance-based correlation analysis of the column chemical compositions to reveal the spatial correlations between various atomic pairs. The detailed chemical information affirms the tendency for like-pair avoidance and unlike-pair preference, specifies the preferred atomic packing and plane stacking by the three constituent species, and suggests a proposed atomic configuration that constitutes the CSRO motif. The fraction of CSRO regions is moderately lowered after either plastic deformation or high-temperature heating. A comparison is also made with previous attempts to identify CSROs in H/MEAs.

1. Introduction

Complex concentrated solution alloys [1] composed of multiple principal elements are currently attracting much attention. They are customarily dubbed as high (or medium)-entropy alloys (HEAs or MEAs) [1–8]. While these H/MEAs are often assumed to be chemically random with configurational entropy approaching that of an ideal solution, it is highly likely that enthalpic interactions among constituent elements would lead to some degree of local chemical order (LCO) at ambient temperatures [9–24], in the otherwise simple-structured lattice, for example, a face-centered cubic (fcc) solution. These LCOs are expected to influence the dynamics of defects (e.g. vacancies, interstitials, and dislocations) in the crystal as well as the macroscopic properties of the alloy [9,10,20-24].

LCOs are on size scales from the atomic level to domains of nanometers. In this work, we focus on the former, i.e., incipient LCOs in the form of chemical short-range order (CSRO) [10,18-24], which, by definition, is prevalent only in the first couple of nearest-neighbor atomic shells. CSRO refers to the preference/avoidance of some of the constituent species in the alloy away from the atomic fractions expected for random mixing, but the chemical order is so short-ranged that it prevails only in the first and the next couple of nearest-neighbor atomic shells around the atom at center. While the presence of CSRO is expected to influence the properties of the alloy such as the dynamics of defects [2,16-18], a convincing identification of CSRO is difficult because of the need to acquire detailed information on atomic scale. It is

* Corresponding authors.
E-mail addresses: xlwu@imech.ac.cn (X. Wu), czy@tsinghua.edu.cn (Z. Cheng), maen@xjtu.edu.cn (E. Ma).
† These authors contributed equally.

https://doi.org/10.1016/j.actamat.2021.117490

these CSRO building blocks that expand/grow in one, two or three dimensions to LCOs on nanometer scale; by then the chemically ordered regions become readily recognizable. The CSROs, on the other hand, are variable and almost always escape detection [9,10], as a convincing identification of CSRO demands intricate chemical information on sub-nanometer length scale, including the occupancy of constituent species on certain lattice planes/sites in the nearest-neighbor environment. One also desires quantitative CSRO order parameters (such as the Warren-Cowley order parameter [25]) and spatial pair correlation functions [26] for each of the several nearest-neighbor atomic shells, to ascertain the preference/avoidance for certain species. Such explicit details are difficult to come by. Even the acquisition of diffraction evidence is a tall order, as the coherent scattering signal from the tiny CSROs is rather weak and may not yield recognizable extra reflection.

The MEA we deal with in this work is the nominally random CrCoNi solution, which is a prototypical fcc MEA widely cited in the community [7,8,10,15,19,22]. A strong case can be made here, to motivate the study of CSROs inside CrCoNi. First, the key attributes of this multicomponent system are that the three species are very similar in atomic size, exhibit rather small heat of mixing, and form no known equilibrium ternary intermetallic compounds over the entire range of temperatures and compositions. One naturally wonders if CSROs can be developed at all, in such a completely soluble system when the composition is in the center of the phase diagram. In this context, CrCoNi can serve as an interesting and general model case for many multi-principal-element complex concentrated alloys [1], for which it is difficult to predict *a priori* if a single-phase H/MEA solution would contain CSROs. Second, if CSROs do develop, it is rather curious what kind of CSRO would emerge, as no chemically ordered metastable state has been predicted as a potential candidate/reference. In such a case, exactly what kind of CSRO would be developed and to what extent are questions that have not been convincingly answered thus far. An in-depth probe into the CSRO in such a system is therefore meaningful and important. Third, the query as to if CSRO actually exists in the CrCoNi case has reached the level of a hot debate in the HEA community. For example, a recent report claimed CSRO in this MEA [10] (the uncertainties associated with this claim will be discussed in Section 3.4), but another paper published at about the same time believed the opposite [23]. In the following, we resolve this challenging issue [9,10,20,23], by employing a full suite of characterization methods, including electron diffraction, atomic-resolution lattice imaging and chemical mapping, as well as modeling calculations. Our dedicated search has found an appropriate zone axis to directly observe CSRO in an aberration-corrected transmission electron microscope (TEM), producing the "seeing is believing" dataset that resolves any possible ambiguity left by Ref. [10] about the CSRO in CrCoNi MEA.

2. Material, processing and experimental methods

The CrCoNi medium-entropy alloy was produced by arc-melting pure chromium, cobalt, and nickel (all >99.9% purity) and subsequently casting into a 130 mm diameter iron mold under an argon atmosphere. To ensure homogeneity, the ingot was re-melted five times. The chemical composition (atomic%) was 33.5% Cr, 32.5% Co, and 34% Ni. The ingot was hot-forged and hot-rolled at 1150 °C to a plate with the dimensions of 12 × 50 × 700 mm^3. The plate was then homogenization-treated in vacuum at 1100 °C for 12 h, followed by rapidly quenching in water. The plate was cold-rolled by 90% thickness reduction to final sheets of 1.0 mm thickness.

Tensile specimens were cut along the rolling direction, with a gauge cross-section of 4 × 1 mm^2 and 15 mm in length. The recrystallization annealing was conducted before tensile straining, at 600 ºC and 1000 ºC, respectively, both for 1 hour. The uniaxial tensile straining was performed using MTS 793 machine at room temperature and a strain rate of 5×10^{-4} s^{-1}.

Thin foils for TEM observations were polished to 50 μm, then punched to discs 3 mm in diameter. Perforation by twin-jet electro-polishing was carried out using a solution of 5 vol% perchloric acid and 95 vol% alcohol, at −25 °C and 30 V. The thin regions in the TEM specimen used for TEM experiments are ~30 nm in thickness. Atomic-resolution TEM and HAADF-STEM were performed on an aberration-corrected scanning transmission electron microscope (FEI Titan Cubed Themis G2 300) operated at 300 kV, equipped with a Super-X EDS with four windowless silicon-drift detectors. The nano beam electron diffraction was performed under the TEM microprobe mode, with the electron beam spot diameter of 35 nm. The image was obtained using Flucam-Viewer with Sensitivity 6. Quantitative energy dispersive X-ray spectroscopy (EDS) mapping with atomic-resolution was conducted on both the samples before and after tensile test. The count rate was in the range of 180 to 500 cps when acquiring atomic-resolution EDS maps. The dwell time was 5 μs per pixel with a map size of 512 × 512 pixels; each EDS mapping took roughly 1 hour to reach the high signal-to-noise ratio.

3. Results and discussion

3.1. Microstructure

Figs. 1a and 1b are the electron back-scattered diffraction images for CrCoNi MEA after recrystallization annealing for 1 hour at 600 °C and 1000 °C, respectively. The resultant microstructure is a single fcc phase in both cases and the average grain size was 1.2 μm and 50 μm, respectively. For the 600 °C-annealed sample, both the TEM and high-resolution TEM imaging (Figs. 1c and 1d), together with the selected-area electron diffraction pattern (EDP), nano beam EDP, and Fast Fourier transform (FFT) in Figs. 1e, 1f and 1g respectively, all with the [110] zone axis (z.a.) as is normally used in previous TEM work to look for the signs of CSROs [9,10], show a normal fcc lattice with no indication of CSROs. If the latter exist at all, their symmetry/packing features do not produce telltale signatures that can be separated out of the information collected under this zone axis. Therefore, various zone axes [27] from the low-index to high-index ones need to be tried, to eventually find the zone axis that can provide the necessary diffraction evidence for the CSRO regions.

3.2. TEM characterization of CSROs

3.2.1. Electron diffraction of CSROs

Interestingly, evidence regarding CSRO emerged when we switched to the [112] z.a. in the 600 °C-annealed sample. The selected-area EDP shows the expected Bragg diffraction spots of the fcc lattice (Fig. 2a). Interestingly, there are weak extra spots, which are highly diffuse with a diameter several times that of the normal Bragg spot, visible in the middle between the transmission spot (000) and the $\{\bar{3}11\}$ spot as indicated by arrows; one example is highlighted using a yellow circle. The presence of a broad intensity maximum can be confirmed by a hump in the measured diffraction intensity along the dashed green line (lower panel). These extra diffuse disks are indications that there are CSRO regions of very small size [28]: it is shown before that when CSRO has a length scale of less than 1 nm, it generates a reflection that would expand to a disk ~5 times the size of a normal reciprocal-lattice spot [28].

Fig. 2b is the high-angle annular dark-field (HAADF) image taken in an fcc grain with the [112] z.a. As shown in inset in Fig. 2b, the FFT pattern clearly exhibits extra superlattice reflections (one is circled in yellow as an example) in between the

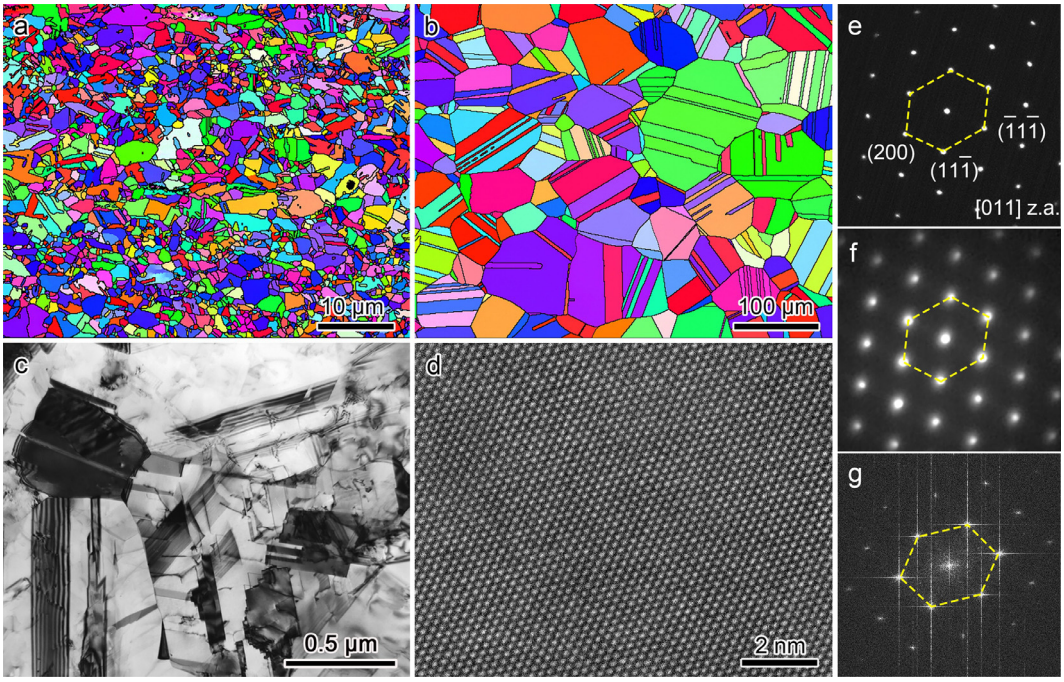

Fig. 1. Microstructure in CrCoNi medium-entropy alloy. (a) and (b) Electron back-scatter diffraction (EBSD) images showing fcc single-phase after recrystallization annealing at 600 °C (a) and 1000 °C (b), respectively, both for 1 hour. (c), (d) TEM and high-resolution TEM images of fcc microstructure in 600 °C-annealed sample. e) - g) Selected-area electron diffraction pattern (EDP), nano beam EDP, and fast Fourier transform pattern, respectively, all with the [110] z.a.

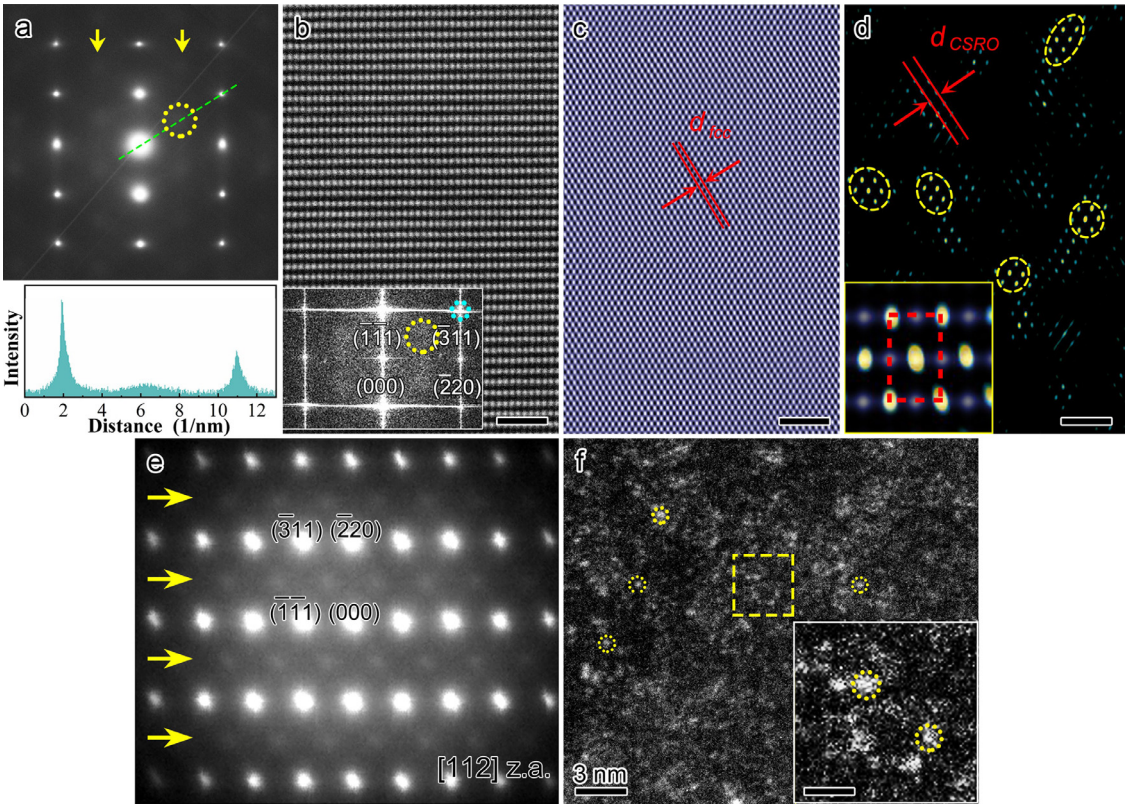

Fig. 2. Evidence of CSRO in 600 °C-annealed sample. (a) Selected-area electron diffraction pattern (EDP) of fcc phase with the [112] z.a. Note the extra discs appearing at $\frac{1}{2}\{\bar{3}11\}$ positions (e.g., the weak disk inside the yellow circle). Lower panel: diffraction intensity along the green dashed line. (b) HAADF lattice image of fcc phase with the [112] z.a. Inset: the corresponding Fast Fourier transform (FFT) pattern showing the extra diffuse reflections (one is labeled by yellow circle) at $\frac{1}{2}\{\bar{3}11\}$ positions, along with sharp Braggs spots from the FCC phase (blue circles). (c) and (d) Inverse FFT images of FCC lattice and CSRO regions (several are circled), respectively. Inset in (d): the close-up view after superimposing two lattices, both with [112] z.a. Overlapping this way produces bright sites that highlight the extra CSRO lining up on $\{\bar{3}11\}$ planes. (e) Nano beam EDP with the [112] z.a. Arrays of superlattice reflections at $\frac{1}{2}\{\bar{3}11\}$ positions as pointed by arrows. (f) Energy-filtered dark-field TEM image taken using extra diffuse disks. Inset: close-up view, highlighting some coherently diffracting CSROs. Throughout this figure, the scale bar is 1 nm unless marked otherwise.

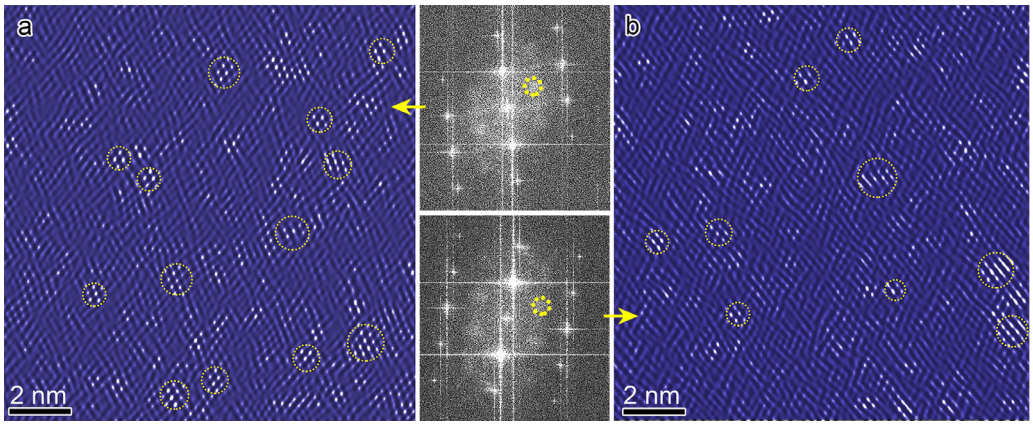

Fig. 3. Inverse FFT image showing CSRO regions (yellow circles). (a) 600 °C-strained sample. (b) 1000 °C-annealed samples. Inset is FFT pattern with the [112] z.a. Note the diffuse reflections (yellow circles) at the positions of $\frac{1}{2}\{\bar{3}11\}$.

transmission spot (000) and the $\{\bar{3}11\}$ diffraction spots. These extra disks are rather diffuse, instead of the sharp diffraction spots which could have other origins [28], and therefore, fiducial indicators of the presence of the CSRO [29–32]. Specifically, because the diameter of diffuse disks in reciprocal space is almost one order of magnitude larger than that of Bragg spots from the fcc lattice, the entities in real space corresponding to these superlattice reflections must be very small in spatial extent [29], at the length scale of *bona fide* CSROs. In general, the presence of CSRO may not necessarily give rise to readily discernable diffraction signals; but when extra reflections are obvious, such as for VCoNi [26] and this CrCoNi MEA, this information in the reciprocal space offers a telltale indicator that CSRO does exist in the solid solution being examined.

Based on the FFT diffraction pattern, two inverse FFT (IFFT) images are obtained. One is the fcc lattice imaged using the normal fcc {311} spots (Fig. 2c), while the other shows the CSRO regions using the diffuse disks (Fig. 2d), where a few CSRO regions are circled in yellow. By comparison, it is visible that the lattice planes characterizing the periodicity of the CSRO (i.e. red lines in Fig. 2d) have an inter-planar spacing (d_{CSRO}) which is twice the interplanar spacing (d_{fcc}) of the normal fcc $\{\bar{3}11\}$ planes (red lines in Fig. 2c). This is the reason why extra reflections appear at the $\frac{1}{2}\{\bar{3}11\}$ positions in the FFT pattern (inset in Fig. 2b). To further ascertain the presence of CSRO, a parallel set of nano beam diffraction experiments were preformed, with the objective aperture diameter of ~35 nm, which is capable to significantly improve the signal-to-noise (background) ratio, along with imaging contrast, as compared to the selected-area diffraction mode. In addition to the expected fcc Bragg spots (indexed), the nano beam EDP (Fig. 2e, still with the [112] z.a.) shows easily discernible extra disks, all lining up still at the positions corresponding to $\frac{1}{2}\{\bar{3}11\}$, as marked using arrows. The observation of extra reflections in both the FFT pattern and nano-beam EDP proves that the fcc CrCoNi MEA contains CSRO regions. To observe the real-space dimension of the coherently scattering CSROs, we obtained the dark-field image (Fig. 2f) taken using the extra disks. The CSRO regions light up.

The CSRO regions were further observed, respectively, in both 600 °C-strained sample after tensile deformation to 18% strain (Fig. 3a) and in 1000 °C-annealed sample (Fig. 3b). Both FFT patterns (insets) again show the extra diffuse disk the same as those shown in the lower panel of Fig. 2a and the inset of Fig. 2b. The IFFT images show the CSRO regions (yellow circles).

Fig. 4 shows the statistic distribution of the size of CSRO regions in three samples. In each of the three cases, more than 300 CSRO regions were counted, respectively, from both the dark-field TEM image and IFFT images. The vast majority (90%) of CSRO regions is less than 1 nm in size. It is interesting that the average size,$\bar{d}$, remains almost unchanged in all three cases (Fig. 4a-c). Such a size scale is what is expected for CSRO regions. However, Fig. 4d shows that the areal fraction, f_{areal}, of the CSRO regions, as measured also from both the dark-field and IFFT images, is different. The f_{areal} decreased from 0.22 to 0.18 after plastic deformation in the 600 °C-annealed sample, and to ~0.16 in the 1000 °C-annealed sample.

3.2.2. EDS-mapping of CSROs

Next, we provide chemical information from representative local regions to ascertain that at least some of the sub-nano entities above indeed contain CSRO that can give rise to the observed extra diffraction signals. This requires a compositional analysis as to exactly what kind of CSRO is present, by probing into the detailed arrangements of the three chemical species (Cr, Co, Ni) in the CSRO regions. To this end, the energy-dispersive X-ray spectroscopy (EDS) mapping was carried out, based on HAADF imaging with the [112] z.a.

We mapped out in the 600 °C-annealed sample, each element, Cr (red), Co (green) and Ni (blue), one by one, as illustrated in the several panels in Fig. 5. Fig. 5a is a HAADF lattice image of fcc grain. The inset is its FFT pattern showing extra disks due to the small CSRO regions. Fig. 5b is the corresponding EDS map. In the image, each spot corresponds to an atomic column along the thickness direction of TEM foil. The intensity (brightness) of colored spots depends on the make-up of the column, scaling with the content of the particular element being probed. Fig. 5c includes one CSRO region (upper-left) and close-up views showing the preferential locations of the three elements in this region. We discover that the CSRO can be best described in terms of Cr occupancy, see the red spots in the Cr map (upper-right in Fig. 5c). Specifically, two Cr-enriched $(\bar{3}11)$ planes (dashed yellow lines, across red spots) sandwich one Cr-depleted $(\bar{3}11)$ plane (in either the Co or the Ni map, under a dashed blue line, across intense green/blue spots but faint or even vanishing red Cr). That is, the Cr-enriched $(\bar{3}11)$ planes alternate with those enriched in Co and/or Ni. Such a chemical order has a period that doubles the interplanar spacing of fcc lattice, and explains again why the diffuse reflections appear at the locations corresponding to $\frac{1}{2}\{\bar{3}11\}$ (both the lower panel of Fig. 2a and inset in Fig. 2b). Furthermore, the alternating preferential chemical occupancy usually extends across only a few $(\bar{3}11)$ planes, i.e. a distance of less than 1 nm, well in line with the size of CSRO regions (Fig. 4). The LCO we observe can hence be rightfully classified as CSRO.

Fig. 6 shows the EDS-maps in 600 °C-strained (Fig. 6a-6c) and 1000 °C-recrystallized (Fig. 6d-6f) samples. In these two cases, in

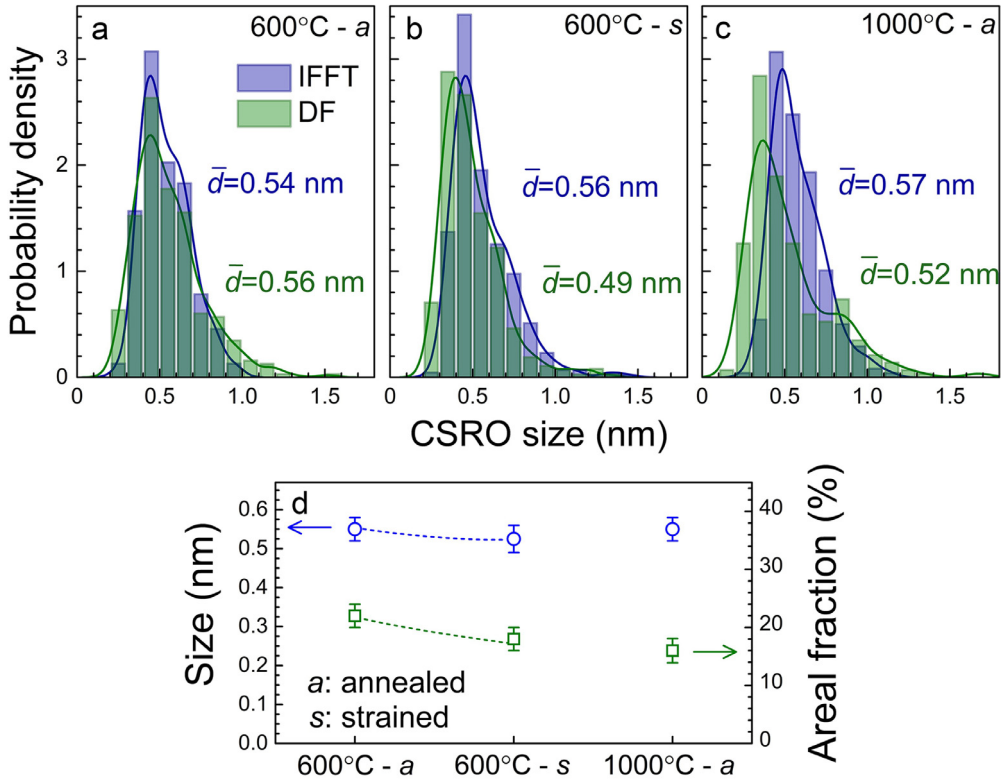

Fig. 4. Change of size and areal fraction of CSRO regions. (a-c) Size distribution of CSROs in three samples. In each of the three cases, more than 300 CSRO regions were counted, respectively, from both the dark-field (DF) TEM image and inverse FFT (IFFT) image. (d) Average size (blue circle) and areal fraction (green square) of the CSRO regions.

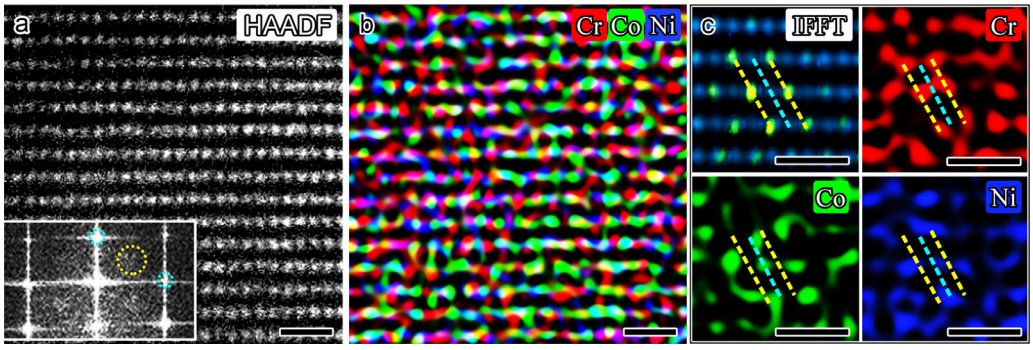

Fig. 5. CSRO and element distribution by EDS mapping in 600 °C-annealed sample. (a) HAADF lattice image of fcc phase with the [112] z.a. Inset: the corresponding Fast Fourier transform (FFT) pattern showing the extra diffuse CSRO reflections (one is labeled by yellow circle) at $\frac{1}{2}\{\bar{3}11\}$ positions. (b) Corresponding EDS map showing the element distribution. (c) IFFT of a specific CSRO region (upper-left) and close-up maps of Cr, Co, and Ni, respectively, for this region. All the dashed lines mark the $(\bar{3}11)$ planes intersecting the (111) plane in plan-view; yellow: Cr-enriched, blue: Co-/Ni- enriched. To be specific, in the Cr map, two Cr-enriched $(\bar{3}11)$ planes (dashed yellow lines, across red spots) sandwich one Cr-depleted $(\bar{3}11)$ plane (in either Co or Ni map, both under a dashed blue line). All scale bars are 0.5 nm.

terms of the occupancy of the three elements in the CSROs, again two Cr-enriched planes are apart by a distance twice the normal spacing of $\{\bar{3}11\}$ planes in fcc lattice, as there is one Co/Ni-enriched plane in-between.

3.2.3. 3D atomic configuration of CSRO

The red dashed rectangle, as shown in the inset of Fig. 2d, is the CSRO motif (Fig. 7a), which led us to conjecture a simplified 3D atomic configuration model of CSRO. The results from the IFFT image and EDS mapping suggest that Cr atoms have a tendency to reside in the eight vertices of unit cell, interspersed with Co/Ni-enriched atomic sites along the [111] direction. This idealized model is presented in Fig. 7b, displaying the alternating $\{\bar{3}11\}$ planes in the [112] projection (Cr-enriched red-ball plane alternating with Co/Ni-enriched green-ball plane). This model has also made use of the line scan chemical mapping profiles along the ⟨110⟩ direction in the {111} plane (see below for the alternating Cr-enriched and Co/Ni-enriched neighboring columns). The simulated EDP with the [112] z.a. for this CSRO, given in Fig. 7c, shows the extra diffuse reflections at the $\frac{1}{2}\{\bar{3}11\}$ positions, which are in full agreement with the selected-area EDP (the upper panel in Fig. 2a), the FFT pattern (the inset in Fig. 2b), and the nano-beam EDP as observed in Fig. 2e. This suggests that such an atomic configuration/ arrangement locally breaks the symmetry of fcc lattice to produce extra reflections, while all Cr, Co and Ni atoms in the CSRO regions still reside on the normal sites of fcc lattice (the color in the motif does not refer to a pure element but only refers to which element is enriched at that location, with a probability above sample-average concentration).

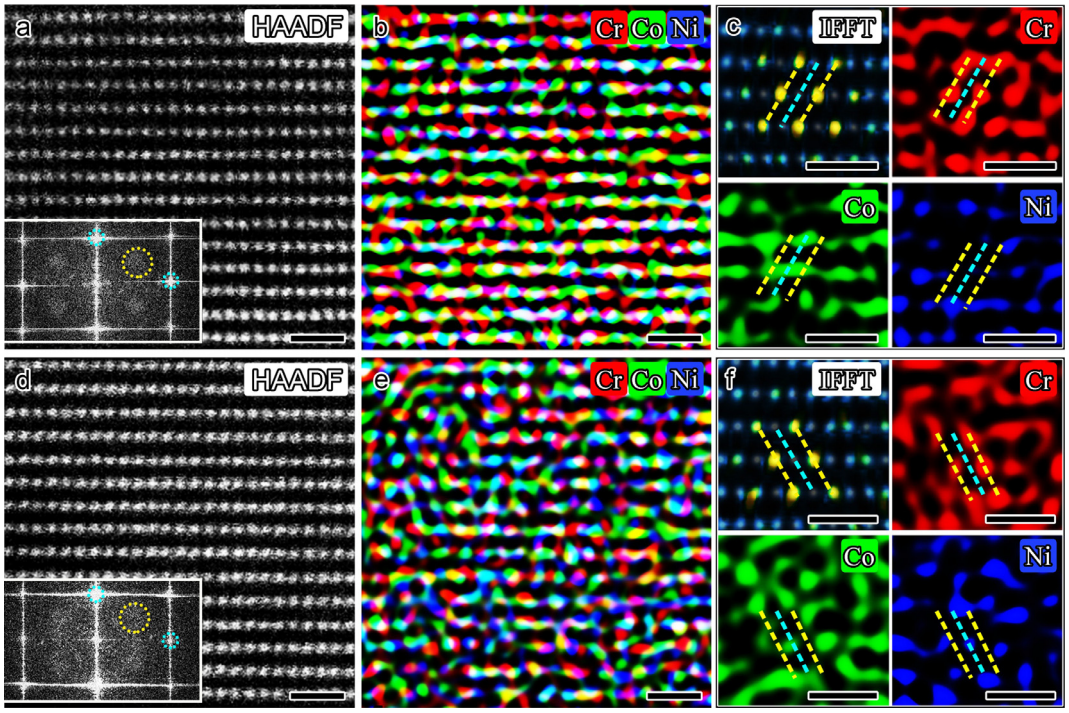

Fig. 6. CSRO region and element distribution by EDS mapping. (a) HAADF image with the [112] z.a. in 600 °C-strained sample. Inset: FFT pattern showing the diffuse CSRO reflections (one is labeled by yellow circle) at $\frac{1}{2}\{\bar{3}11\}$ positions. (b) Corresponding EDS map of the three species. (c) IFFT of a specific CSRO region (upper-left) and close-up maps of Cr, Co, and Ni, respectively, for this CSRO. All dashed lines mark the $(\bar{3}11)$ planes intersecting the (111) plane in plan-view; yellow: Cr-enriched, blue: Co-/Ni- enriched. (d-f) Corresponding results in 1000 °C-annealed sample. All scale bar is 0.5 nm.

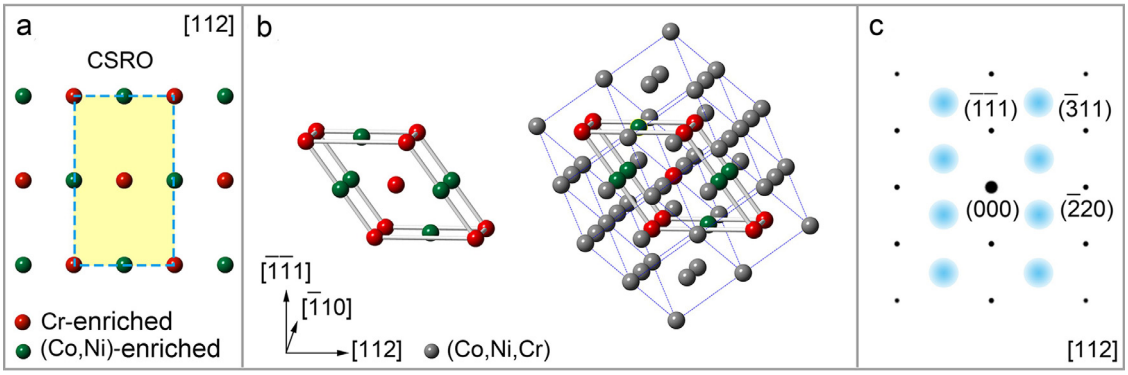

Fig. 7. Schematic 3D atomic configuration of the CSRO motif. (a) Idealized model viewed from the [112] z.a., which captures the alternating $\{\bar{3}11\}$ planes (in the [112] projection, red-ball plane alternating with green-ball plane) - the salient chemical enrichment featured in Fig. 2c and its inset, as well as the alternating columns in [110] direction. (b) Local 3D configuration showing CSRO region in fcc lattice. (c) Corresponding EDP with the [112] z.a.

Furthermore, it is noted that the pattern/CSRO is clearly different from that expected for familiar ordered structures such as $L1_2$, $L1_0$, B2, etc. This finding is instructive, as it demonstrates that the CSRO can present a new (sometimes metastable) structure that is perhaps unexpected and hard to predict *a priori*. In this CrCoNi case, the CSRO resembles the structure of a computationally purported trigonal CrNi phase [33]. Interestingly, this CSRO motif is similar to that in VCoNi MEA [26], where the CSRO appears to be based on a metastable trigonal VNi structure [34]. A discussion comparing the CrCoNi with VCoNi cases will be presented in Section 3.4.

3.3. Quantitatively gaging CSROs from experimental EDS maps

3.3.1. Locating the atomic columns in EDS line profiles

As the next step, we devise a robust method for quantitatively analyzing the chemical preferences from information contained in the experimental EDS maps. In our recent work [26], we developed a pair correlation analysis scheme and demonstrated that the spatial correlation coefficient at the 1st peak/valley is indicative of CSROs in the nearest-neighboring shell. The analysis gauges the degree of spatial correlation between the concentrations of species in the atomic columns, to reflect the spatial correlation between each pair of species, e.g., the tendency for A and B to be neighbors. What is needed, therefore, is the chemical concentration measured from EDS mapping in each atomic column. However, pronounced lattice distortions can be present in the H/MEAs, making it difficult to pinpoint the location of each column (i.e., which signals should be counted as belonging to a particular column). This introduces non-trivial noise and uncertainty to the pair correlation analysis. As an example, in Figs. 5 and 6, although the atomic columns are distinguishable visually, obvious lattice distortions can be observed. Ideally, only the concentrations at the location of atomic columns should be included in the calculation of correlation coeffi-

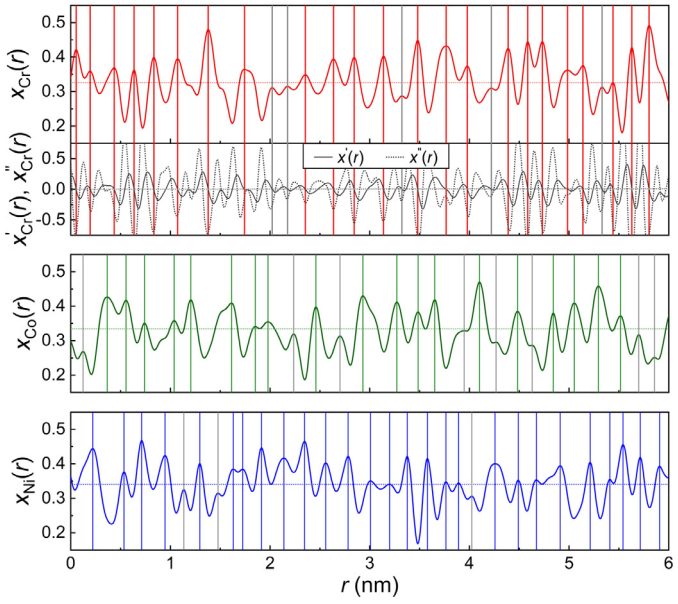

Fig. 8. Locating the element-enriched columns in EDS line profiles. Typical composition line profiles, x_A (A = Cr, Co and Ni), are illustrated, which are obtained from experimental line scans of one (111) plane from EDS mapping. The red, green and blue vertical lines show the determined locations of Cr-, Co- and Ni-enriched columns. The 1st derivative, $x'_A(r)$, and 2nd derivative, $x''_A(r)$, scaled at 0.1 and 0.01 times, respectively, are illustrated for the Cr concentration profile as an example. The gray lines are the excluded local maxima with concentration lower than the sample average of each element (the colored dotted horizontal line).

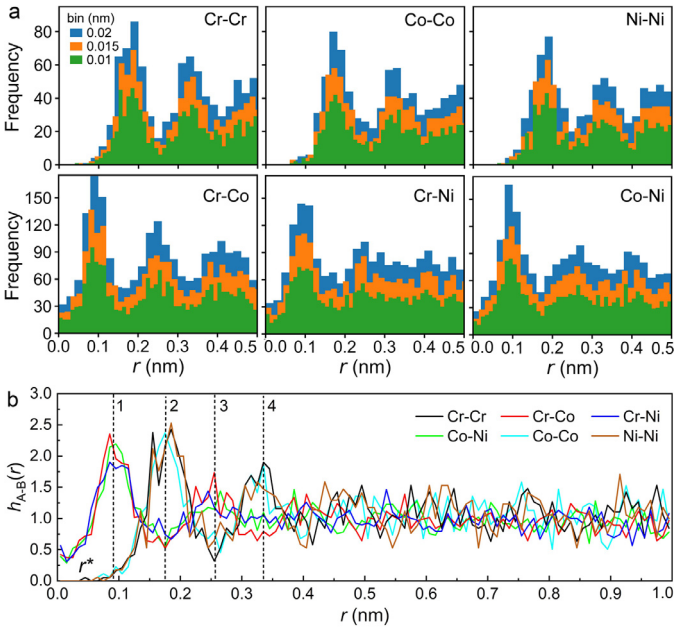

Fig. 9. Probability distribution of the distance between A-enriched and B-enriched columns in 600 °C annealed sample. A (or B) stands for any one of the three constituent species. A total of 20 independent EDS lines are included in the statistics (see Section 2.3 for more details). (a) Histogram plot shows the frequency (number) of column pairs within each distance bin (three representative bin widths are shown). (b) Normalized histograms in (a) so that the area under each histogram integrates to unity. Dashed vertical lines denote the center of four distinct peaks (maxima). The interval between peaks, r^*, gives the distance between neighboring projected atomic columns in (111) plane along [112] z.a.

cient. Thus, in the following we start with a more reliable method to better identify the location of each atomic column in the EDS line profiles. The procedure to locate atomic columns from EDS line profiles with lattice distortions is as follows:

i) Interpolate a spline representation of discrete atomic concentration points covered in an EDS line scan [35]. The resultant concentration profile for species A (A = Cr, Co or Ni), $x_A(r)$, allows for the calculation of derivatives at any location, r.
ii) Calculate the 1st derivative, $x'_A(r)$, and 2nd derivative, $x''_A(r)$ of the concentration profile.
iii) Locate the A-enriched columns (peaks) by employing the following criteria: $x'_A(r) = 0$, $x''_A(r) < 0$ and $x_A(r) > \overline{x_A}$. $\overline{x_A}$ is the average of A concentration in the measured EDS region.

Note that we only care about the local maxima, as the minima can correspond either to A-depleted columns or to the void space between columns (which is not what we want). For the former case, the column locations can then be located from the maxima of the other elements, e.g., when A-depleted the column would be enriched with B and/or C.

To demonstrate the above, Fig. 8 analyzes the concentration profiles along an EDS line scan. Again, the A-enriched columns (peaks) are located using the three criteria, i.e., $x'_A(r) = 0$, $x''_A(r) < 0$ and $x_A(r) > \overline{x_A}$. The 1st and 2nd derivatives, $x'_A(r)$ and $x''_A(r)$, are shown for the Cr concentration profile in Fig. 8 as an example. The red, green and blue vertical lines show the locations of Cr-, Co- and Ni-enriched columns along an EDS line profile. This explicit determination of the locations for the atomic columns enables a more reliable statistical analysis of their spatial distribution and correlation.

3.3.2. Spatial distribution functions

After identifying the Cr-, Co- and Ni-enriched columns and their locations, we further analyze whether they (i.e., these columns of various identity, namely, enriched in different species) distribute with some pattern in space. To this end, we plot the distribution of the distance between A-enriched and B-enriched columns, from a total of 20 independent EDS lines of the 600 °C-annealed sample, where the A-B pair can be any two out of Cr, Co and Ni (Fig. 9).

The histogram plot in Fig. 9a shows the frequency (number) of column pairs within each distance bin (three representative bin widths are shown). For ease of comparison between different column pairs, the histograms in Fig. 9a are normalized such that the area under each histogram integrates to unity (Fig. 9b). This probability density distribution is akin to the partial pair correlation function commonly used to gauge A-B atomic pair distribution correlations in 3D atomic structures. Four distinct peaks (maxima of humps) are observed (their locations are marked with dashed vertical lines in Fig. 9b), before the distribution curve levels off at larger distances. The interval between peaks, r^*, is the distance between neighboring projected atomic columns, in (111) planes when viewed along the [112] z.a., see Fig. 10 for a schematic illustration. It is interesting to find that the columns enriched with the same element, Cr-Cr, Co-Co and Ni-Ni, mostly separate by distances of $2r^*$ and $4r^*$, while the unlike species, Cr-Co and Cr-Ni and Co-Ni, tend to be first-neighbor columns (at r^*, repeating at $3r^*$). This pattern from the line scan is again a manifestation of the CSRO tendency towards like-pair avoidance and unlike pair preference, as already seen in the alternating A-enriched and A-depleted (B/C-enriched) (311) planes in Fig. 5. Both the 600 °C-strained and 1000 °C-annealed samples show the same trend (Fig. 11). In the next step, we will conduct spatial correlation analysis to further quantify the correlation strength in each sample.

3.3.3. Gauging the strength of spatial correlations

To quantitatively gauge the strength of spatial correlation, in a recent work [26], we have defined a set of spatial correlation coef-

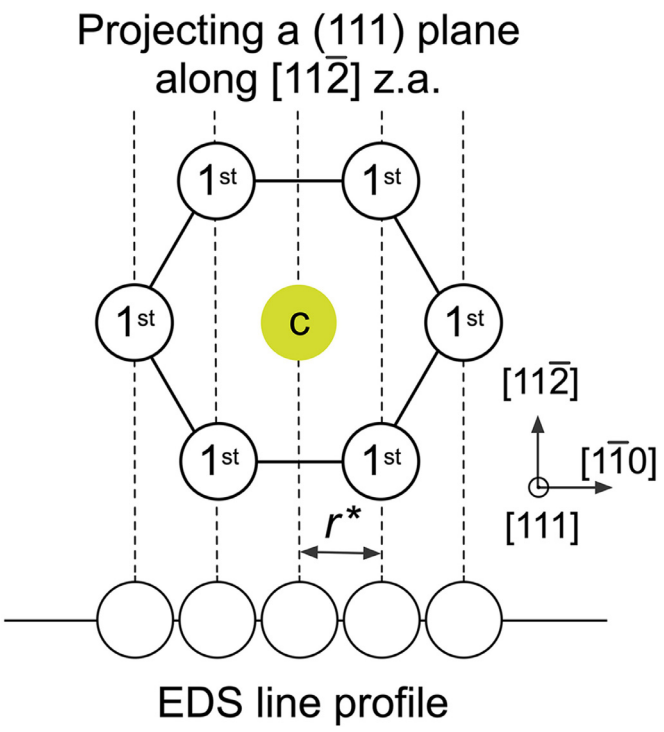

Fig. 10. Schematic of projecting a (111) plane along [11$\bar{2}$] zone axis. The six spheres marked as "1st" illustrates the 1st-neighbors of the center atom (blue sphere marked as "c"). r^* corresponds to the projected distance between neighboring columns on the (111) plane viewed along [11$\bar{2}$] z.a.

ficient, $C_{A-B}(r)$, between an A-B element pair:

$$C_{A-B}(r) = \frac{\langle (x_A(0) - \langle x_A \rangle)(x_B(r) - \langle x_B \rangle) \rangle}{\sqrt{\langle (x_A - \langle x_A \rangle)^2 \rangle}\sqrt{\langle (x_B - \langle x_B \rangle)^2 \rangle}} \quad (1)$$

where $x_A(0)$ is the atomic concentration of element A at reference position (0) in an EDS line profile and $x_B(r)$ is the concentration of B a distance of r away, and $\langle x_A \rangle$ and $\langle x_B \rangle$ are the average chemical composition of A and B, respectively.

A positive $C_{A-B}(r)$ indicates that the compositions with r apart tend to vary synchronously. A negative $C_{A-B}(r)$ signals a negative correlation, i.e., the two are inversely correlated. When A and B are of the same species, $C_{A-B}(r)$ characterizes the self-correlation of that element at r; when not, they characterize the cross-correlation between different species. In this form of covariance normalized by the product of standard deviations, the correlation coefficient $C_{A-B}(r)$ falls in $[-1, 1]$ and is robust in indicating the correlation strength between A and B at distance r apart.

Now that we have the atomic column positions, we no longer use all the concentration values across the entire line profile, i.e., any pair of concentrations at two locations separated by any distance r. Instead we only use the concentrations corresponding to the identified atomic columns (using the method presented in 3.3.1) for the calculation of $C_{A-B}(r)$. This is an improvement over the method used in our recent paper [26], as it weeds out spurious noise associated with local displacements arising from lattice distortion and drift during EDS data acquisition. The robustness of our correlation analysis is enhanced as a result. Specifically, in calculating $C_{A-B}(r)$, we followed these five steps:

i) For each EDS line, follow the procedures described in 3.3.1 to reliably determine the location of the Cr/Co/Ni-enriched columns;
ii) Along the EDS line, mark all the column locations. A given column can be enriched in either Cr, Co or Ni. This union set of all these Cr-, Co- and Ni-enriched columns therefore represent all the column locations in the EDS line scan. Columns that are too close-by (with distance < 0.015 nm) are merged: for example, one column is enriched with both Co and Ni, but the identified Co- and Ni-enriched locations are slightly shifted from each other; in this case, the latter two will be merged as one column by taking their mid-point;
iii) Derive the corresponding concentrations, $x_{Cr}(r)$, $x_{Co}(r)$ and $x_{Ni}(r)$, at each of all the identified column locations for use in the calculation of $C_{A-B}(r)$ at various column separation distances;
iv) Repeat i) to iii) for all the EDS lines available. Here, a total of 20 EDS lines are included for the 600 °C sample before and after straining, and 14 EDS lines are included for the 1000 °C sample. This extensive sampling ensures a sufficiently large data set for the later correlation strength analysis.
v) Calculate the correlation coefficients, $C_{A-B}(r)$, at $r = r^*$, $2r^*$, $3r^*$ and $4r^*$. As the distance between atomic columns in EDS maps is actually a distribution (over a range) instead of a single number (as seen in Figs. 9 and 11), the distance between columns is in the form of "peak envelope", each having a width and being bounded by valleys on either side. The peak envelope covering a range is therefore designated as representing the atomic column in question. Based on Fig. 9b, we designate the distance ranges of the 1st, 2nd, 3rd and 4th peak envelopes as [0.07, 0.13], [0.15, 0.21], [0.23, 0.29], [0.30, 0.36] (in nm), respectively. We proceed to sample all the A-B concentration pairs at distances within the 1st, 2nd, 3rd and 4th peak envelopes, and use Eq. (1) to calculate the $C_{A-B}(r^*)$, $C_{A-B}(2r^*)$, $C_{A-B}(3r^*)$ and $C_{A-B}(4r^*)$. In a nutshell, these values gauge the degree of spatial correlation between the concentrations of species in the atomic columns at the locations of interest, and as such reflect the spatial correlation between each pair of species, i.e., the tendency for A and B to be preferred or avoided when separated by multiples of inter-columnar spacing.

Fig. 12 shows the calculation results of C_{A-B} at various separation distances. Again, only the chemical concentrations and locations of atomic column pairs identified within the peak range (around r^*, $2r^*$, $3r^*$ and $4r^*$, see Fig. 9b) are used to evaluate $C_{A-B}(r)$. Obvious peaks and valleys exist in the $C_{A-B}(r)$ curves. For each of the three sample states, Cr-Cr, Co-Co and Ni-Ni exhibit a negative $C(r^*)$. This indicates that the like elements are inclined not to be nearest neighbors. The unlike species, especially for Cr-Co and Cr-Ni, on the other hand, appear to attract each other, giving rise to positive $C(r^*)$. This chemical ordering tendency was found before in DFT-guided Monte Carlo simulations of CrCoNi [12,19], which explained the preference for unlike pairs and avoidance of like pairs from the energy reduction perspective. Meanwhile, although the enthalpic interaction between Co and Ni is relatively weak, i.e., weaker than that involving Cr, there is still a tendency towards chemical ordering, with Co-Ni being preferred and Co-Co and Ni-Ni avoided, in a statistical sense. In general, we see an alternating negative and positive $C(r^*)$ that persists at 1, 2, 3 and 4 times the distance r^* (Fig. 12). Such a repeating/alternating sequence is reminiscent of our observations in Figs. 5 and 6.

The amplitudes (absolute values) of $C_{A-B}(r^*)$ show a systematic decrease (except for an increase for Cr-Ni) in the 600 °C-strained sample, see Fig. 12. This suggests a modest decrease of the degree of CSRO regions. This is in line with the reduced areal fraction of CSRO regions after tensile straining (Fig. 4d). During plastic flow, some CSRO regions are destructed due to dislocation slip that would shear the atomic planes to force the solution towards random, attenuating the spatial pair correlations. For the 1000 °C-annealed sample, the magnitudes of $C_{Cr-Cr}(r^*)$, $C_{Cr-Co}(r^*)$ and $C_{Co-Co}(r^*)$ decrease by comparison to the 600 °C-annealed

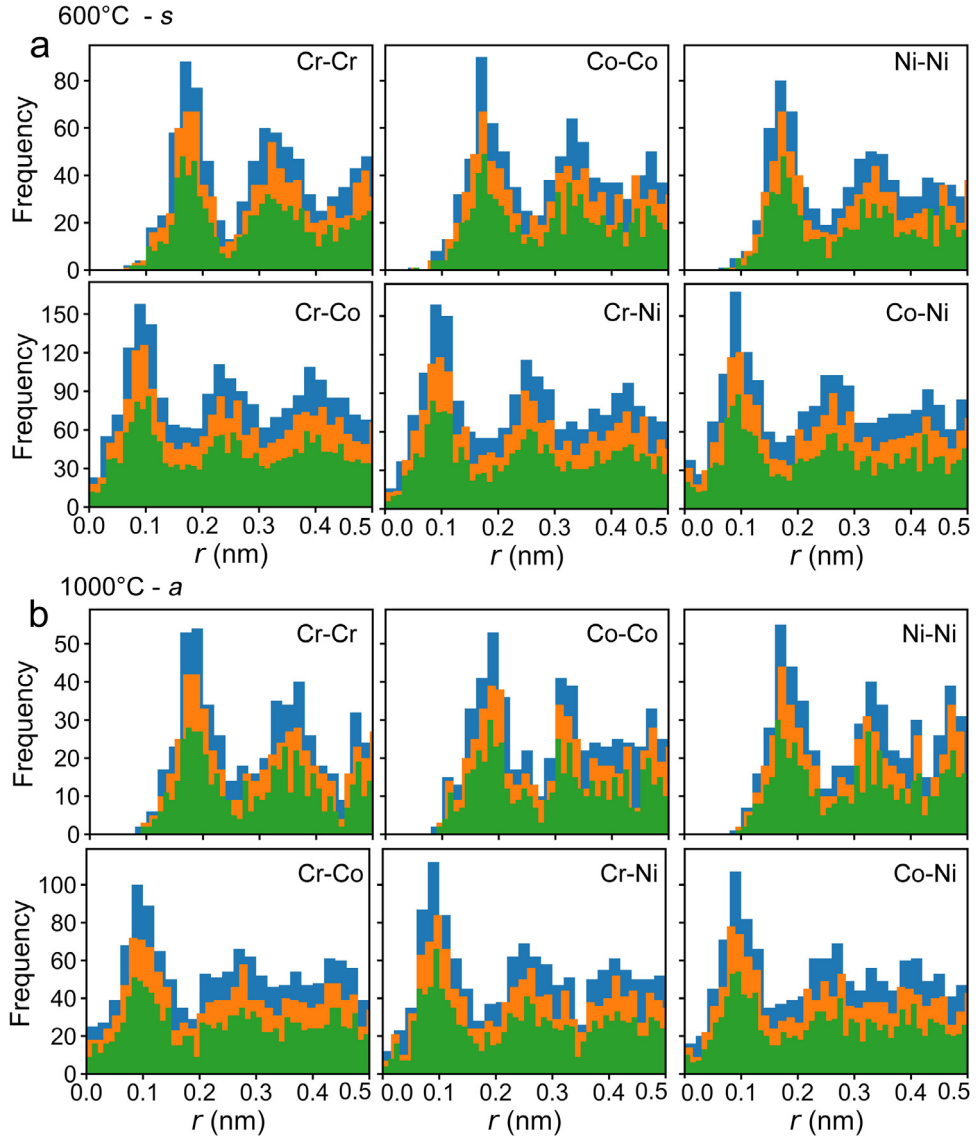

Fig. 11. Probability distribution for the distance between A-enriched and B-enriched columns in 600 °C-strained sample (a) and 1000 °C-annealed (b). A total of 20 and 14 independent EDS lines are included in the statistics for the two samples, respectively. The histogram plot shows the frequency (number) of column pairs within each distance bin (three representative bin widths are shown).

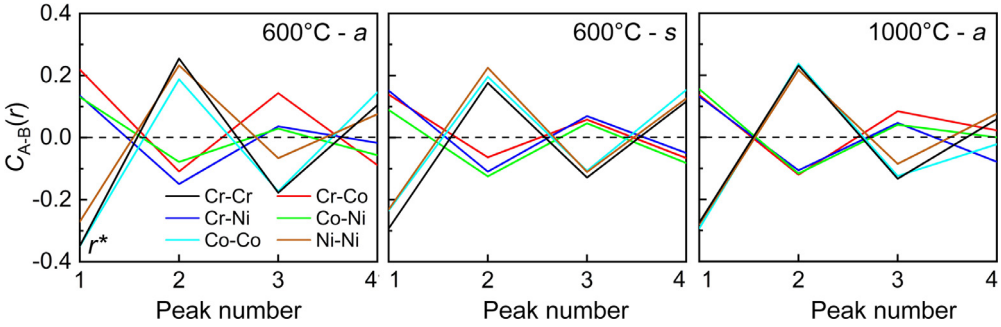

Fig. 12. Quantifying the strength of spatial correlation. Spatial pair correlation coefficients, $C_{A-B}(r)$, between the six element pairs, for three CrCoNi samples.

sample, see Fig. 12. Actually, a lesser degree of CSRO is expected at a higher temperature. The enthalpic interaction would play a less role in driving the CSRO at high temperatures when entropic effects become more dominant. However, the CSROs remain obvious even at 1000 °C (Fig. 12), suggesting a strong tendency to form CSROs in CrCoNi.

3.4. Comparing with previous pursuit of CSRO in H/MEAs

Although a number of studies have been devoted to detecting CSROs in H/MEAs over the past several years, firm evidence has remained sorely missing [11–18]. Almost all experiments [13-15,18] had to rely on indirect approaches such as fitting of X-ray

or neutron data, often requiring extensive computation, to make the claim. Very recently, Zhang et al. [10] claimed to have obtained TEM evidence of CSRO in the CrCoNi MEA, and Seol et al. [27] also claimed the existence of CSRO in fcc-based non-equiatomic FeMnCrCo HEA and compared it to long-range ordered precipitate [27]. But their methods are different from ours, and their work has left much to be desired for. To see this, we emphasize that there are two fundamental aspects when it comes to identifying CSRO. First of all, one must affirm that the local chemical order is indeed short-ranged. CSRO, by definition, refers to the preference/avoidance for certain species over the sample-average atomic fraction, often characterized by a finite short-range order parameter, for the first and second nearest-neighbor atomic shells, i.e., on a length scale below ~1 nm in real space. This is very different from the long-range periodicity that would give sharp spots in reciprocal (diffraction) space [28]. In other words, for the tiny CSRO coherently diffracting domain, based on the definitive real-reciprocal space relationship/correspondence, the most direct evidence in diffraction pattern one could hope to detect are extra disks that are highly diffuse, at locations corresponding to the CSRO. This is exactly what we have demonstrated using diffraction and FFT patterns, while Ref. [10] only showed streaking on diffraction spots. There is no theoretical basis to confirm that the long (one dimensional) streaks of the diffraction spot uniquely identify nanometer-diameter domains corresponding to CSRO. The streaks are instead more common to planar defects, such as stacking faults. Ref. [10] also showed some ~5 nm regions. But even if such domains can be proven to be chemically ordered regions, the dimension of several nanometers is obviously well beyond the length scale of CSROs, although these could be local chemical order grown up from CSRO to persist over a local region with dimensions ~5 nm. Note that our success requires proper selection of zone axis, which our search managed to achieve via a series of experimental trials in various e-beam directions. In imaging, we actually see the chemical order on {113} planes under [112] zone axis, as well as atomic columns in the [110] direction that prefer different species in an alternating fashion. Also, using dark-field imaging from these diffuse disks, we have clearly shown the spatial extent of the (sub-nanometer) CSRO regions in real space.

Second, even if one accepts that the evidence in Ref. [10] is indicative of the presence of CSRO, to nail down CSRO one must also report what kind of chemical order it is. That is, one must have the chemical information as to how the constituent elemental species reside in the neighboring atomic shell/plane(s), with different tendencies to preferentially occupy certain lattice planes/sites. There has been no such information from Ref. [10] or other prior experimental work on H/MEAs [28]. In this regard, we captured quantitative information using atomic-resolution EDS, and developed robust pair correlation analyses to characterize the strength of spatial correlation. In the absence of such details, it would not be able to resolve the ongoing debate or even controversy regarding CSRO in the H/MEA field.

Very recently, the presence of CSRO has been detected in VCoNi MEA [26]. A comparison between the VCoNi with CrCoNi is therefore in order. First, we notice that the extra diffuse reflections arising from the CSRO in CrCoNi have lower intensity than those from the CSRO in VCoNi. This seems to suggest that the degree of CSRO in CrCoNi is lower than that in VCoNi, which is expected since the VCoNi system has a larger negative heat of mixing, and the ternary and sub-systems (binaries) are known to form ordered intermetallic phases. The same cannot be said for CrCoNi, which has no known ternary compounds. Also, Cr, Co and Ni are very close in atomic number and size, also contributing to the super-lattice reflections being less intense. Second, it is interesting to find that the CSRO configurations in VCoNi and CrCoNi appear to be isomorphous. The VCoNi CSRO configuration has been found to bear resemblance to that of metastable VNi. From this perspective the CrCoNi CSRO configuration may not seem to be entirely a surprise, because one form of CrNi can also have the same trigonal crystal structure as VNi in the Materials Project database [33,34]. However, the formation energy is negative for VNi but positive for CrNi, which, while lending support to the VNi-type structure in VCoNi, is suggestive of a low likelihood of the trigonal-CrNi-centric metastable structure in CrCoNi. The other possible explanation of the CSRO observed in CrCoNi is that the configuration may be related to the somewhat complex cubic Laves structure of $CrNi_2$ [36], which does have a slightly negative formation energy and is on convex hull. From this standpoint, one could perhaps picture Co as Ni, such that CrCoNi would locally have a tendency to organize towards $CrNi_2$. However, a concrete connection between these two structures remains to be established.

4. Summary

In sum, in this paper we have shown for the H/MEA community a clear-cut experiment, to provide irrefutable identification of CSRO in a prototypical MEA-CrCoNi. The direct observation of CSRO in CrCoNi MEA was made possible by exploiting an appropriate zone axis, nano beam diffraction, dark-field imaging, atomic-resolution HAADF-STEM with FFT and IFFT, and atomic-scale EDS composition map. Furthermore, we have devised a quantitative analysis to pinpoint the locations of atomic columns and construct distribution functions, as well as coefficients to gauge spatial correlations. This approach is expected to be useful for the community to evaluate CSRO and spatial correlations by extracting information from the concentration profiles in EDS chemical maps. The combination of these complementary tools/methods avoided missing links or interference from artifacts, allowing us to conclusively demonstrate CSRO in a MEA. In this regard, the equi-atomic CrCoNi adds an exemplary case of multi-principal-element complex concentrated alloys [1], as a single-phase H/MEA solution but containing CSROs that have not been (or even cannot be) predicted *a priori*. The CSRO is known to favor planar slip of dislocations [9]. In general, CSRO is expected to interact with moving dislocations [26], changing their glide pattern and hence the shape of the stress-strain curve including the strain hardening behavior in a mechanical property test.

Declaration of Competing Interest

The authors declare that they have no known competing financial interests or personal relationships that could have appeared to influence the work reported in this paper.

Acknowledgement

This work is supported by the Ministry of Science and Technology of China (Grant No. 2019YFA0209900), NSFC (Grant Nos. 11972350, 11890680, and 11988102) and the Chinese Academy of Sciences (Grant No. XDB22040503). E.M. thanks XJTU for hosting his work at CAID.

References

[1] D.B. Miracle, O.N. Senkov, A critical review of high entropy alloys and related concept, Acta Mater 122 (2017) 448–511.
[2] E.P. George, W.A. Curtin, C.C. Tasan, High entropy alloys: a focused review of mechanical properties and deformation mechanisms, Acta Mater 188 (2020) 435–474.
[3] E. Ma, X.L. Wu, Tailoring heterogeneities in high-entropy alloys to promote strength-ductility synergy, Nat. Commun. 10 (2019) 5623.
[4] Z.M. Li, K.G. Pradeep, Y. Deng, D. Raabe, C.C. Tasan, Metastable high-entropy dual-phase alloys overcome the strength-ductility trade-off, Nature 534 (2016) 227–230.
[5] Z. Lei, X. Liu, Y. Wu, H. Wang, S. Jiang, S. Wang, X. Hui, Y. Wu, B. Gault, P. Konits, et al., Enhanced strength and ductility in a high-entropy alloy via ordered oxygen complexes, Nature 563 (2018) 546–550.

[6] S.L. Wei, S.J. Kim, J.Y. Kang, Y. Zhang, Y.J. Zhang, T. Furuhara, E.S. Park, C.C. Tasan, Natural-mixing guided design of refractory high-entropy alloys with as-cast tensile ductility, Nat. Mater. 19 (2020) 1175–1181.
[7] M.X. Yang, D.S. Yan, F.P. Yuan, P. Jiang, E. Ma, X.L. Wu, Dynamically reinforced heterogeneous grain structure prolongs ductility in a medium-entropy alloy with gigapascal yield strength, Proc. Natl. Acad. Sci. U.S.A. 115 (2018) 7224–7229.
[8] C.E. Slone, J. Miao, E.P. George, M.J. Mills, Achieving ultra-high strength and ductility in equiatomic CrCoNi with partially recrystallized microstructures, Acta Mater 165 (2019) 496–507.
[9] Q.Q. Ding, Y. Zhang, X. Zhang, X.Q. Fu, D.K. Chen, S.J. Chen, L. Gu, F. Wei, H.B. Bei, Y.F. Gao, et al., Tuning element distribution, structure and properties by composition in high-entropy alloys, Nature 574 (2019) 223–227.
[10] R.P. Zhang, S.T. Zhao, J. Ding, Y. Chong, T. Jia, C. Ophus, M. Asta, R.O. Ritchie, A.M. Minor, Short-range order and its impact on the CrCoNi medium-entropy alloy, Nature 581 (2020) 283–287.
[11] M. Widom, W.P. Huhn, S. Maiti, W. Steurer, Hybrid Monte Carlo/Molecular Dynamics Simulation of a Refractory Metal High Entropy Alloy, Metall. Mater. Trans. A 45 (2014) 196–200.
[12] A. Tamm, A. Aabloo, M. Klintenberg, M. Stocks, A. Caro, Atomic-scale properties of Ni-based FCC ternary, and quaternary alloys, Acta Mater 99 (2015) 307–312.
[13] L.J. Santodonato, Y. Zhang, M. Feygenson, C.M. Parish, M.C. Gao, R.J.K. Weber, J.C. Neuefeind, Z. Tang, P.K. Liaw, Deviation from high-entropy configurations in the atomic distributions of a multi-principal-element alloy, Nat. Commun. 6 (2015) 5964.
[14] P. Singh, A.V. Smirnov, D.D. Johnson, Atomic short-range order and incipient long-range order in high-entropy alloys, Phys. Rev. B 91 (2015) 224204.
[15] F.X. Zhang, S.J. Zhao, K. Jin, H. Xue, G. Velisa, H. Bei, R. Huang, J.Y.P. Ko, D.C. Pagan, J.C. Neuefeind, W.J. Weber, Y.W. Zhang, Local Structure and Short-Range Order in a NiCoCr Solid Solution Alloy, Phys. Rev. Lett. 118 (2017) 205501.
[16] L. Koch, F. Granberg, T. Brink, D. Utt, K. Albe, F. Djurabekova, K. Nordlund, Local segregation versus irradiation effects in high-entropy alloys: steady-state conditions in a driven system, J. Appl. Phys. 122 (2017) 105106.
[17] A. Fernández-Caballero, J.S. Wróbel, P.M. Mummery, D. Nguyen-Manh, Short--Range Order in High Entropy Alloys: theoretical Formulation and Application to Mo-Nb-Ta-V-W System, J. Phase Equilib. Diffus. 38 (2017) 391–403.
[18] Y. Ma, Q. Wang, C.L. Li, L.J. Santodonato, M. Feygenson, C. Dong, P.K. Liaw, Chemical short-range orders and the induced structural transition in high-entropy alloys, Scr. Mater. 144 (2018) 64–68.
[19] J. Ding, Q. Yu, M. Asta, R.O. Ritchie, Tunable stacking fault energies by tailoring local chemical order in CrCoNi medium-entropy alloys, Proc. Natl. Acad. Sci. U.S.A. 115 (2018) 8919–8924.
[20] Q.J. Li, H. Sheng, E. Ma, Strengthening in multi-principal element alloys with local-chemical-order roughened dislocation pathways, Nat. Commun. 10 (2019) 3563.
[21] H.S. Oh, S.J. Kim, K. Odbadrakh, W. Ha Ryu, K.N. Yoon, S. Mu, F. Kormann, Y. Ikeda, C.C. Tasan, D. Raabe, T. Egami, E.S. Park, Engineering atomic-level complexity in high-entropy and complex concentrated alloys, Nat. Commun. 10 (2019) 2090.
[22] W.R. Jian, Z.C. Xie, S.Z. Xu, Y.Q. Su, X.H. Yao, I.J. Beyerlein, Effects of lattice distortion and chemical short-range order on the mechanisms of deformation in medium entropy alloy CoCrNi, Acta Mater 199 (2020) 352–369.
[23] B.L. Yin, S. Yoshida, N. Tsuji, W.A. Curtin, Yield strength and misfit volumes of NiCoCr and implications for short-range-order, Nat. Commun. 11 (2020) 2507.
[24] Y. Wu, F. Zhang, X.Y. Yuan, H.L. Huang, X.C. Wen, Y.H. Wang, H.H. Wu, X.J. Liu, H. Wang, S.H. Jiang, Z.P. Lu, Short-range ordering and its effects on mechanical properties of high-entropy alloys, J. Mater. Sci. Technol. 62 (2021) 214–220.
[25] B.E. Warren, X-Ray Diffraction, Reprint, Dover Publications, New York, 1990.
[26] X.F. Chen, Q. Wang, Z.Y. Cheng, M.L. Zhu, H. Zhou, P. Jiang, L.L. Zhou, Q.Q. Xue, F.P. Yuan, J. Zhu, X.L. Wu, E. Ma, Direct observation of chemical short-range order in a medium-entropy alloy, Nature 592 (2021) 712–716.
[27] J.W.Bae J.B.Seol, H.Sung J.G.Kim, H.H.Lee Z.M.Li, J.H.Jang S.H.Shim, S.I.Hong W.-S.Ko, H.S. Kim, Short-range order strengthening in boron–doped high-entropy alloys for cryogenic applications, Acta Mater 194 (2020) 366–377.
[28] J. Reyes-Gasga, A. Gómez-Rodríguez, X.X. Gao, M. José-Yacamán, On the interpretation of the forbidden spots observed in the electron diffraction patterns of flat Au triangular nanoparticles, Ultramicroscopy 108 (2008) 929–936.
[29] D.B. Williams, C.B. Carter, Transmission Electron Microscopy, A Textbook For Materials Science, Springer, New York, 2009.
[30] N. Kuwano, N. Chiwata, K. Oki, In situ TEM observation of long range ordering via short range order in Cu3Pt, Bull. Mater. Sci. 22 (1999) 697–700.
[31] G.Van Tendeloo, S. Amelinckx, The origin of diffuse intensity in electron diffraction patterns, Phase Transit 67 (1998) 101–135.
[32] S.K. Young, Y.M. Wan, S.K. Sung, Effect of short-range ordering on stress corrosion cracking susceptibility of Alloy 600 studied by electron and neutron diffraction, Acta Mater 83 (2015) 507–515.
[33] The Materials Project, https://materialsproject.org/materials/mp-1226232/.
[34] The Materials Project, https://materialsproject.org/materials/mp-1216313/.
[35] C.R. Harris, K.J. Millman, S.J.V.D. Walt, R. Gommers, P. Virtanen, D. Cournapeau, E. Wieser, J. Taylor, S. Berg, N.J. Smith, R. Kern, M. Picus, S. Hoyer, M.H.V. Kerkwijk, M. Brett, A. Haldane, J.F.D. Rio, M. Wiebe, P. Peterson, P.G. Marchant, K. Sheppaard, T. Reddy, W. Weckesser, H. Abbasi, C. Gohlke, T.E. Oliphant, Array programming with NumPy, Nature 585 (2020) 357–362.
[36] The Materials Project, https://materialsproject.org/materials/mp-784631/.